doi.org/10.26434/chemrxiv.13382069.v1

Computational Study of Inverted All-Inorganic Perovskite Solar Cells Based on CsPbIxBr3-X Absorber Layer with Band Gap of 1.78 eV

Nahuel Martínez, Carlos Pinzón, Guillermo Casas, Fernando Alvira, Marcelo Cappelletti

Submitted date: 15/12/2020 • Posted date: 21/12/2020

Citation information: Martínez, Nahuel; Pinzón, Carlos; Casas, Guillermo; Alvira, Fernando; Cappelletti, Marcelo (2020): Computational Study of Inverted All-Inorganic Perovskite Solar Cells Based on CsPbIxBr3-X Absorber Layer with Band Gap of 1.78 eV. ChemRxiv. Preprint.
https://doi.org/10.26434/chemrxiv.13382069.v1

All-inorganic perovskite solar cells (PSCs) with inverted p-i-n configuration have not yet reached the high efficiency achieved in the normal n-i-p architecture. However, the inverted all-inorganic PSC are more compatible with the fabrication of tandem solar cells. In this work, a theoretical study of all-inorganic PSCs with inverted structure ITO/HTL/$CsPbI_xBr_3$–x/ETL/Ag, has been performed by means of computer simulation. Four p-type inorganic materials (NiO, Cu_2O, CuSCN and CuI) and three n-type inorganic materials (ZnO, TiO_2 and SnO_2) were used as hole and electron transport layers (HTL and ETL), respectively. A band gap of 1.78 eV was used for the CsPbI x Br_3–x perovskite layer. The simulation results allow identifying that CuI and ZnO are the most appropriate materials as HTL and ETL, respectively. Additionally, optimized values of thickness, acceptor density and defect density in the absorber layer have been obtained for the ITO/CuI/CsPbI x Br_3–x /ZnO/Ag, from which, an optimum efficiency of 21.82% was achieved. These promising theoretical results aim to improve the manufacturing process of inverted all-inorganic PSCs and to enhance the performance of perovskite–perovskite tandem solar cells.

File list (1)

ChemRXiv Perovskitas Wang.pdf (463.28 KiB) view on ChemRxiv • download file

Computational study of inverted all-inorganic perovskite solar cells based on $CsPbI_xBr_{3-x}$ absorber layer with band gap of 1.78 eV

Nahuel Martínez[1,2], Carlos Pinzón[1], Guillermo Casas[1], Fernando Alvira[1], Marcelo Cappelletti[3,4]

[1] Universidad Nacional de Quilmes, Science and Technology Department, Laboratorio de BioNanotecnología (LBN) Roque Sáenz Peña 352, Bs. As, Argentina. Zip: 1876.

[2] CIFICEN (UNCPBA-CICPBA-CONICET), Pinto 399, (7000) Tandil, Argentina.

[3] Grupo de Control Aplicado (GCA), Instituto LEICI (UNLP-CONICET), Facultad de Ingeniería, Universidad Nacional de La Plata, C.C.91 (1900), La Plata, Argentina.

[4] Programa TICAPPS, Universidad Nacional Arturo Jauretche, Av. Calchaquí 6200 (1888), Florencio Varela, Argentina.

E-mail: nahuelm@exa.unicen.edu.ar

Abstract

All-inorganic perovskite solar cells (PSCs) with inverted p-i-n configuration have not yet reached the high efficiency achieved in the normal n-i-p architecture. However, the inverted all-inorganic PSC are more compatible with the fabrication of tandem solar cells. In this work, a theoretical study of all-inorganic PSCs with inverted structure ITO/HTL/$CsPbI_xBr_{3-x}$/ETL/Ag, has been performed by means of computer simulation. Four p-type inorganic materials (NiO, Cu_2O, CuSCN and CuI) and three n-type inorganic materials (ZnO, TiO_2 and SnO_2) were used as hole and electron transport layers (HTL and ETL), respectively. A band gap of 1.78 eV was used for the $CsPbI_xBr_{3-x}$ perovskite layer. The simulation results allow identifying that CuI and ZnO are the most appropriate materials as HTL and ETL, respectively. Additionally, optimized values of thickness, acceptor density and defect density in the absorber layer have been obtained for the ITO/CuI/$CsPbI_xBr_{3-x}$/ZnO/Ag, from which, an optimum efficiency of 21.82% was achieved. These promising theoretical results aim to improve the manufacturing process of inverted all-inorganic PSCs and to enhance the performance of perovskite–perovskite tandem solar cells.

Keywords:
All-inorganic perovskite solar cells
$CsPbI_xBr_{3-x}$ thin films (bad gap of 1.78 eV)
SCAPS-1D simulation
Power conversion efficiency
Optimization

1. Introduction

The increase in energy consumption promotes the use of new technologies based on renewable energy sources to generate electricity, with solar energy being one of the most promising alternatives. In this sense, the study of solar cells, devices capable of converting light from the sun directly into electricity, is extremely important today. At the same time, the study of microscopic properties of materials, in addition to advances in the manufacturing processes of the photovoltaic devices, has provided a path to develop new technologies in solar cells with higher power conversion efficiency (*PCE*) and shorter processing time.

One of the developments that have gained special relevance in recent years are perovskite solar cells (PSCs), which have emerged as a technology with the potential to revolutionize the photovoltaic industry. This is mainly due to their excellent optical and electronic properties such as tunable band gap, large absorption coefficient, high charge carrier mobility and long diffusion lengths, and their simpler fabrication process and lower cost compared to conventional crystalline silicon solar cell (Burschka et al., 2013; Gao et al., 2014; Gonzalez-Pedro et al., 2014; Grätzel, 2014; Karthick et al., 2020; Saliba et al., 2016; Stranks et al., 2013; Yang and You, 2017).

In general, PSCs consist of a perovskite layer as a light-absorbing region sandwiched between a p-type hole-transporting layer (HTL) and an n-type electron-transporting layer (ETL). HTL allows the free flow of holes towards the anode but blocks electron flow. On the contrary, the ETL block holes flow but allow the free flow of electrons towards the cathode.

PSCs with the HTL/Perovskite/ETL structure have substantially increased their *PCE* from 3.8% in 2009 (Kojima et al., 2009) to 25.5% recently in 2020 (NREL, 2020). The highest efficiencies so far were obtained for the so-called organic–inorganic hybrid perovskite-based solar cells using $MAPbX_3$ as perovskite layer, where MA is the methylammonium cation ($MA^+ = (CH_3NH_3)^+$) and X is a halide anion (Cl^-, Br^- or I^-). These devices have achieved efficiencies comparable to technologies already established in the market, such as thin film solar cells based on cadmium telluride (CdTe) or copper indium gallium selenide (CIGS), or even, as silicon solar cells. However, the long-term stability of organic–inorganic hybrid perovskite-based solar cells is sensitive to water and moisture due to the high volatility of hydrophilic organic cations (i.e. $CH_3NH_3^+$), which is a strong obstacle for their further development and commercial applications (L. Chen et al., 2019a; Conings et al., 2015).

The substitution of the volatile organic compounds with cesium (Cs^+) is one of the alternatives that have recently begun to be explored and that has proven to be very effective in order to prevent degradation and improve stability of the PSCs, which makes them very attractive for further study (Liu et al., 2018; Sutton et al., 2016; Wang et al., 2020). In the last years, several works have been reported in the literature dedicated to improving the performance of $CsPbI_xBr_{3-x}$ based PSCs, with x between 0 and 3 (Jiang et al., 2018; Li et al., 2018; Swarnkar et al., 2016; Tian et al., 2019; Wang et al., 2017). From the variation of x values, it is possible to tune the band gap of $CsPbI_xBr_{3-x}$ in the range between 1.73 eV and 2.31 eV for $CsPbI_3$ and $CsPbBr_3$, respectively (Tao et al., 2019). In particular, $CsPbI_3$ based PSCs have significantly enhanced the efficiency from 2.9% (Eperon et al., 2015) to 19.03% (Wang et al., 2019). In addition, an optimum efficiency of 21.31% has been obtained for these devices by numerical simulation (Lin et al., 2020). On the other hand, efficiencies of 16.2% (Tian et al., 2019), 10.9% (Subhani et al., 2019) and 10.6% (Zhao et al., 2019) have been reported for $CsPbI_2Br$, $CsPbIBr_2$ and $CsPbBr_3$ based PSCs, respectively.

Most of the high-performance all-inorganic PSCs reported so far are based in the normal n-i-p architecture due to their superiority in performance (W. Chen et al., 2019; Tian et al., 2019). However, the study and development of all-inorganic PSCs with inverted p-i-n structure has become very attractive due to these devices are more compatible with the fabrication of perovskite–perovskite tandem solar cells (Beal et al., 2016; Zhang et al., 2018), whose efficiencies can be improved by optimizing the design of each inverted all-inorganic PSCs separately. For instance, inverted $CsPbI_xBr_{3-x}$ based PSC (band gap of 1.78 eV) with a *PCE* of 15.6% was recently reported, where a Lewis base small molecule was used to passivate the inorganic perovskite film (Wang et al., 2020). Also, inverted all-inorganic $CsPb_{1-x}Ni_xI_2Br$ (x = 0−0.1) PSC with a *PCE* of 13.88% was reported (L. Chen et al., 2019b). These *PCE* values are still well below the 25.2% of organic–inorganic hybrid PSCs, therefore, further studies of inverted all-inorganic PSCs are really very desirable in order to explore the factors that limit its performance and to obtain higher efficiencies than reported so far.

In this work, a comparative analysis of different combinations of inverted all-inorganic PSCs based on $CsPbI_xBr_{3-x}$ as perovskite layer, with band gap of 1.78 eV, has been carried out by means of computer simulation. Modeling and simulation techniques are fundamental tools to predict and analyze the behavior of the devices under study. Additionally, from these tools it is

possible to investigate the relationship between the internal physical mechanisms and material properties with device performance. Four materials (NiO, Cu_2O, CuSCN and CuI) have been proposed as inorganic hole-transporting layer (i-HTL); and three materials (ZnO, TiO_2 and SnO_2) were used as inorganic electron-transporting layer (i-ETL). These seven inorganic materials under consideration in this study have different physical parameters, such as band gap energies, electron affinities, carrier mobilities, among others, and they are promising candidates for use in all-inorganic PSCs with inverted structure. The devices performance was theoretically evaluated for different thicknesses, acceptor densities and defect densities in the perovskite layer, to optimize the design of the structure and to enhance the efficiency of these inverted all-inorganic PSCs.

2. Simulation details

Simulations were performed with SCAPS-1D software (Burgelman et al., 2000), which is widely used and recognized by the scientific community related to PSCs (Adhikari et al., 2016; Chakraborty et al., 2019; Haider et al., 2019; Lin et al., 2020). This software numerically solves the three coupled differential equations: the Poisson and the continuity equations for electrons and holes. The output parameters such as short-circuit current density (J_{SC}), open circuit voltage (V_{OC}), power conversion efficiency (*PCE*), maximum power point (P_{MAX}), fill factor (*FF*) and external quantum efficiency (*EQE*), can be calculated using the SCAPS-1D software, in order to obtain the response of the device under different design and operating conditions. Some of the authors of this paper have previously used SCAPS-1D to study the organic–inorganic hybrid PSCs (Cappelletti et al., 2018; Casas et al., 2017).

Fig. 1 shows the configuration of the all-inorganic PSC used in this work, which consists of an inverted structure ITO/i-HTL/$CsPbI_xBr_{3-x}$/i-ETL/Ag, where light enters through the i-HTL. The standard AM1.5G spectrum (1000 W/m^2; T =300°K) has been used.

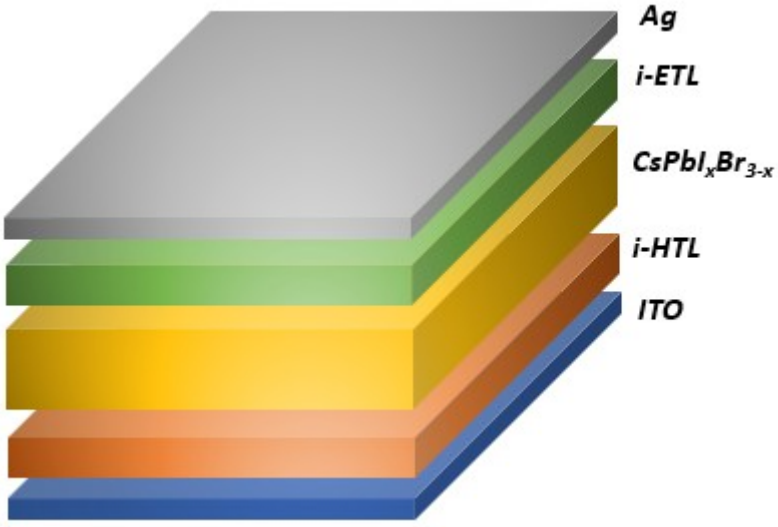

Fig. 1. Device architecture of inverted all-inorganic PSC used in this work.

Tables 1-3 summarize the main parameters used in the simulations for the perovskite layer, and for the materials chosen as i-HTL and i-ETL, respectively, where N_A and N_D are the acceptor and donor density, respectively; ε_r is the relative permittivity; χ is the electron affinity; E_G is the band gap energy; μ_n and μ_p are the electron and hole mobilities, respectively; N_T is the defect density; and N_C and N_V are the effective conduction and valence band density of states, respectively. These values are based on experimental and theoretical studies recently reported in the literature (Lin et al., 2020; Wang et al., 2020). For example, a band gap of 1.78 eV was used for the $CsPbI_xBr_{3-x}$ thin film, like that reported in (Wang et al., 2020). The value of

2.07×10^{14} cm^{-3} for the N_T in the perovskite layer was chosen to obtain a carrier diffusion length of 1 µm, which is a similar value to the one used in Dastidar 2017 and Lin 2020 (Dastidar et al., 2017; Lin et al., 2020). The absorption coefficient (α) used for the $CsPbI_xBr_{3-x}$ layer was calculated from the Beer-Lambert law $\alpha = 2.303A/t$ (Nama Manjunatha and Paul, 2015), where A and t are absorbance and thickness of film (350 nm), respectively, which were obtained from Wang 2020 (Wang et al., 2020). The absorption coefficient as a function of the wavelength for the $CsPbI_xBr_{3-x}$ layer used in this paper is shown in Fig. 2. The work functions of the front and back contacts are 4.7 eV (ITO) and 4.26 eV (Ag), respectively (Behrouznejad et al., 2016).

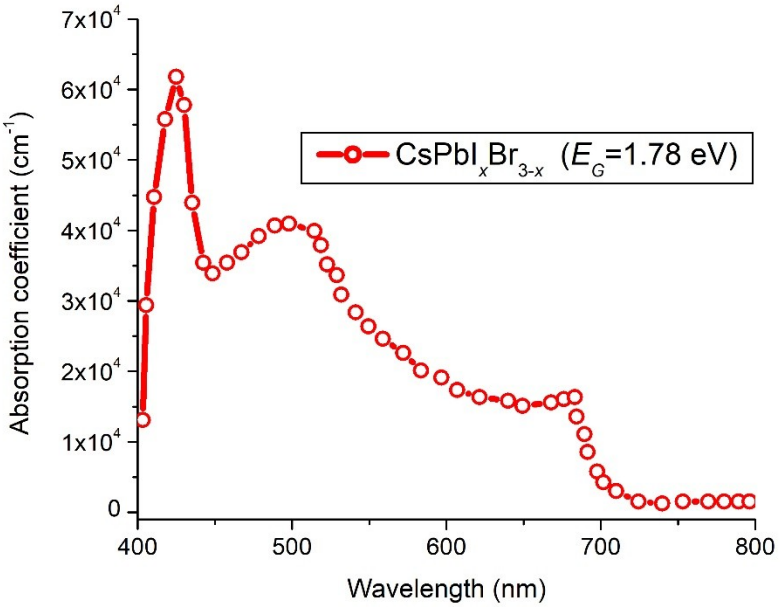

Fig. 2. Absorption coefficient values of $CsPbI_xBr_{3-x}$ film used in this work versus wavelength.

Table 1.
Physical parameters of the perovskite material used in the simulation.

Parameters	$CsPbI_xBr_{3-x}$
Thickness (nm)	350
N_A (cm^{-3})	1×10^{15}
N_D (cm^{-3})	-
ε_r	6
χ (eV)	3.95
E_G (eV)	1.78
μ_n ($cm^2V^{-1}s^{-1}$)	16
μ_p ($cm^2V^{-1}s^{-1}$)	16
N_T (cm^{-3})	2.07×10^{14}
N_C (cm^{-3})	1.1×10^{20}
N_V (cm^{-3})	8×10^{19}

Table 2.
Physical parameters of the i-HTL materials used in the simulation.

Parameters	NiO	Cu_2O	CuSCN	CuI
Thickness (nm)	25	25	25	25
N_A (cm^{-3})	3×10^{18}	3×10^{18}	3×10^{18}	3×10^{18}
N_D (cm^{-3})	-	-	-	-
ε_r	11.7	7.11	10	6.5
χ (eV)	1.46	3.2	1.9	2.1
E_G (eV)	3.8	2.17	3.4	3.1
μ_n ($cm^2V^{-1}s^{-1}$)	2.8	200	2×10^{-4}	100
μ_p ($cm^2V^{-1}s^{-1}$)	2.8	80	2×10^{-1}	44
N_T (cm^{-3})	1×10^{17}	1×10^{17}	1×10^{17}	1×10^{17}

N_C (cm^{-3})	2.5×10^{20}	2.5×10^{20}	1.7×10^{19}	2.8×10^{19}
N_V (cm^{-3})	2.5×10^{20}	2.5×10^{20}	2.5×10^{21}	1×10^{19}

Table 3.
Physical parameters of the i-ETL materials used in the simulation.

Parameters	ZnO	TiO_2	SnO_2
Thickness (nm)	25	25	25
N_A (cm^{-3})	-	-	-
N_D (cm^{-3})	3×10^{18}	3×10^{18}	3×10^{18}
ε_r	9	9	9
χ (eV)	4	4	4
E_G (eV)	3.16	3.2	3.5
μ_n (cm^{2}V^{-1}s^{-1})	100	20	20
μ_p (cm^{2}V^{-1}s^{-1})	25	10	10
N_T (cm^{-3})	1×10^{17}	1×10^{17}	1×10^{17}
N_C (cm^{-3})	4.5×10^{18}	1×10^{21}	4.36×10^{18}
N_V (cm^{-3})	1×10^{18}	2×10^{20}	2.52×10^{19}

Fig. 3 shows, the values with respect to the vacuum level, of the Minimum of the Conduction Band (MCB) and of the Maximum of the Valence Band (MVB) for the i-ETL and i-HTL materials used in the simulation, respectively. MCB and MVB values are also observed for the $CsPbI_xBr_{3-x}$ layer with a band gap of 1.78 eV.

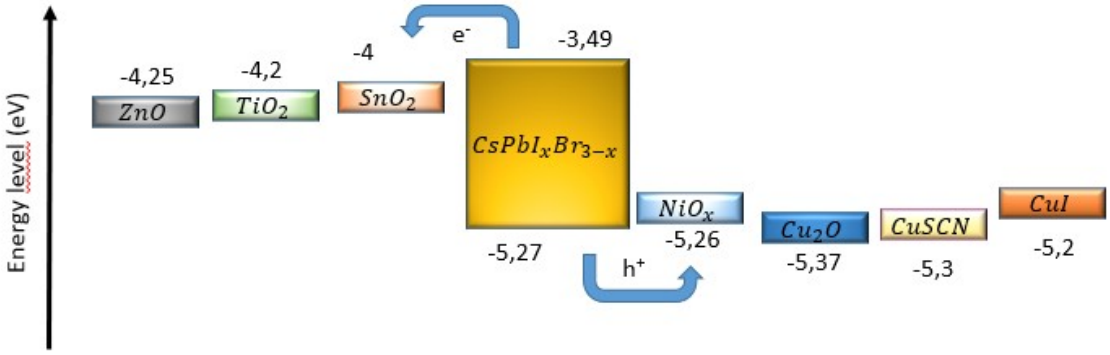

Fig. 3. Energy-level diagram of the studied inverted all-inorganic PSC with different i-ETL and i-HTL.

3. Results and discussion

First, an analysis of the twelve different possible combinations (i-ETL/i-HTL) of the inverted all-inorganic PSCs was carried out based on the physical parameters presented in Tables 1-3. The results of the output parameters are summarized in Table 4. In particular, the first row in this table corresponds to the materials used in (Wang et al., 2020). The value of *PCE* of 11.77% obtained from simulations for the ZnO/NiO combination, can be considered as a good first approximation to the experimental results presented there for the control device with the non-passivated perovskite film. Although in Wang 2020 (Wang et al., 2020), a value of *PCE* of 13.9% is mentioned, a histogram of *PCE* values over 32 PSCs is presented in the supplementary material, where the *PCE* values are approximately between 11.5% and 13.9%.

Table 4.
Output parameters of the PSC for the twelve different combinations considered in this work.

i-ETL / i-HTL	J_{SC} (mA/cm^2)	V_{OC} (V)	*FF* (%)	*PCE* (%)
ZnO / NiO	13.44	1.13	77.55	11.77

SnO_2 / NiO	13.42	1.13	77.55	11.75
TiO_2 / NiO	13.44	1.12	77.24	11.67
ZnO / Cu_2O	12.98	1.13	78.44	11.53
SnO_2 / Cu_2O	12.97	1.13	78.44	11.51
TiO_2 / Cu_2O	12.98	1.12	78.49	11.47
ZnO / CuSCN	13.44	1.14	73.25	11.19
SnO_2 / CuSCN	13.42	1.14	73.26	11.18
TiO_2 / CuSCN	13.44	1.13	72.24	11.01
ZnO / CuI	13.46	1.13	78.61	11.96
SnO_2 / CuI	13.45	1.13	78.61	11.94
TiO_2 / CuI	13.46	1.12	78.50	11.89

It can also be observed in Table 4 that J_{SC} and V_{OC} values remain almost unchanged for the twelve cases, whereas *FF* and *PCE* are the most fluctuating parameters, approximately 9% between their minimum and maximum values. The lowest *FF* and *PCE* values are obtained for the three PSCs based on CuSCN as HTL, which is mainly due to the low hole mobility of CuSCN compared to the other materials. Therefore, CuSCN is not the optimal material as HTL for $CsPbI_xBr_{3-x}$ based PSCs as considered in this work. On the contrary, the three PSCs with CuI as HTL show the highest *FF* and *PCE* values. In order to study in more detail the *PCE* variation as a function of the hole mobility, simulations varying this parameter were carried out. Fig. 4 shows results obtained when the hole mobility is varied from 2×10^{-5} to 200 $cm^2V^{-1}s^{-1}$, whereas the other values of Table 2 have remained unchanged. Only three i-ETL/i-HTL combinations are plotted in this figure for clarity. A critical hole mobility value near 10 $cm^2V^{-1}s^{-1}$ can be observed, below which *PCE* is significantly reduced up to around 8%. On the contrary, *PCE* remains constant for values of hole mobility larger than 10 $cm^2V^{-1}s^{-1}$.

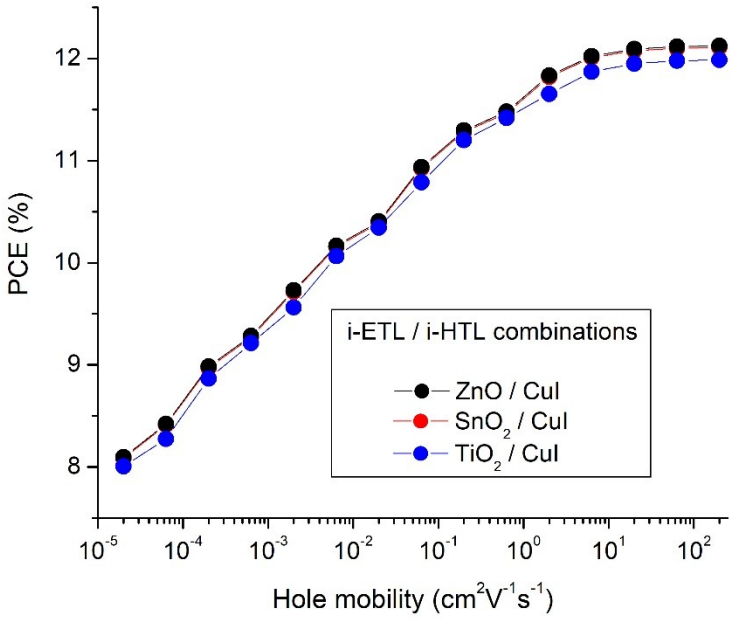

Fig. 4. Power conversion efficiency versus hole mobility for three i-ETL/CuI combinations considered in this work.

In particular, the highest *PCE* value of 11.96% was observed for the ZnO/CuI combination. Although the theoretical results presented in Table 4 were obtained using a thickness of 350 nm for $CsPbI_xBr_{3-x}$ layer, a similar qualitative behavior was observed for higher thicknesses.

Later, new simulations on the PSC with the inverted structure of ITO/CuI/$CsPbI_xBr_{3-x}$/ZnO/Ag have been performed, using different thicknesses, acceptor densities and defect densities for the perovskite layer. The study was focused on this layer, in which light is absorbed to produce photo-generated carriers, thus playing a decisive role in the device performance.

In Fig. 5 is plotted the simulated current density-voltage (J-V) characteristics of the solar cell for three different thicknesses of the absorber film: 350, 750 and 1050 nm. Compared to the

originally analyzed thickness (350 nm), a slight reduction in V_{OC} but a significant increase in J_{SC} were obtained for the other two devices. This result is shown more clearly in Fig. 6, in which the variation of the electrical parameters (*PCE*, V_{OC} and J_{SC}) as a function of the $CsPbI_xBr_{3-x}$ thickness can be observed. The values presented in this figure are normalized to those corresponding to their maximum values, which are 16.06%, 1.15 V, and 23.79 mA/cm^2, for *PCE*, V_{OC} and J_{SC}, respectively. In the case of the *PCE* parameter, a strong increase is also seen when the thickness is increased from 250 to 750 nm, but for thicknesses greater than 750 nm the *PCE* values have remained almost unchanged. Regarding these results, a value of 750 nm is considered as the optimized value in what follows.

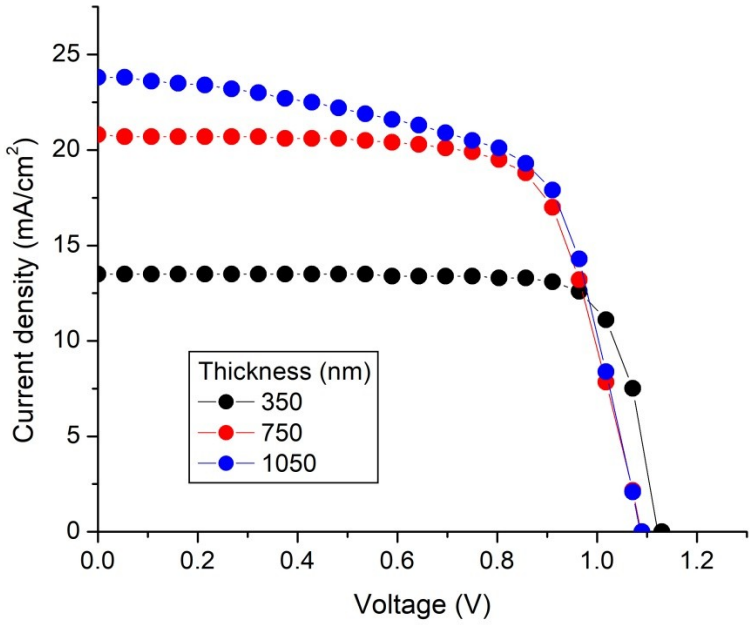

Fig. 5. J-V characteristics with three different thicknesses of the perovskite layer.

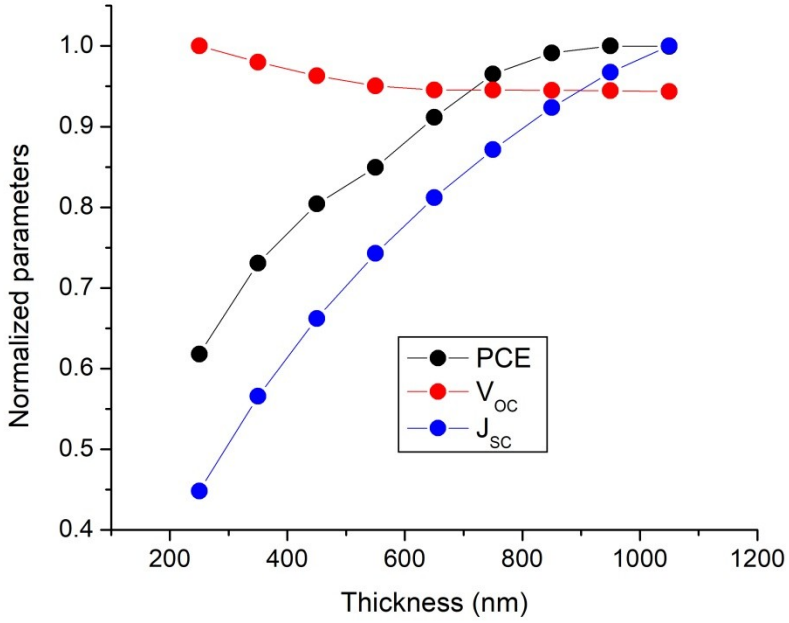

Fig. 6. Normalized electrical parameters as a function of the perovskite thickness.

On the other hand, Fig. 7 shows the variation of *PCE* as a function of the acceptor density in the perovskite layer. As can be seen in this figure, for the range of values considered here, a significant reduction in *PCE* occurs when N_A is varied from 10^{14} to 10^{16} cm^{-3}.

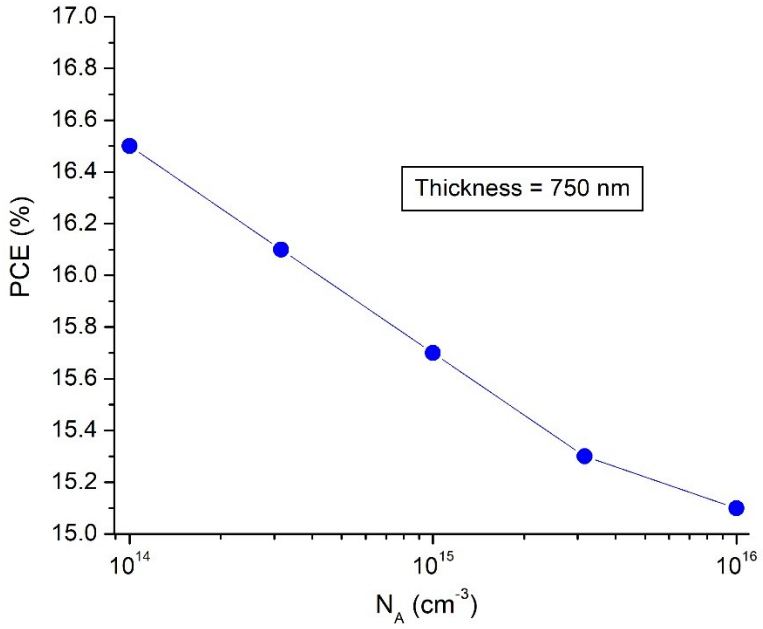

Fig. 7. *PCE* as a function of N_A.

Finally, the defect density of perovskite layer has a significant impact on device performance, such as is shown in Fig. 8 for two different cases: one for the initial values presented in Table 1 (red circles), and other assuming the optimized values obtained in previous step, that is: thickness (t) = 750 nm and N_A = 10^{14} cm^{-3} (blue circles). The simulation results show that for a minority-carrier diffusion length of 1 µm (N_T = 2.07 × 10^{14} cm^{-3}), the *PCE* value increases from 11.96% to 16.34% when optimized parameters are used. Finally, this figure also shows the performance improvement that could be achieved by reducing the defect density. Specifically, for the extreme case of N_T = 2.07 × 10^{12} cm^{-3} (that is minority-carrier diffusion length of 10 µm) an optimum efficiency of 21.82% can be obtained for the inverted device with a structure of ITO/CuI/$CsPbI_xBr_{3-x}$/ZnO/Ag.

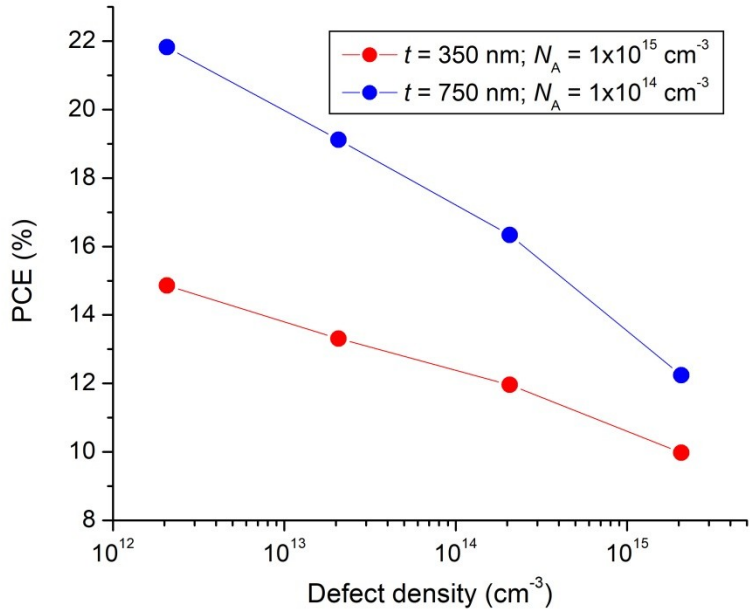

Fig. 8. *PCE* variation with respect to the defect density of $CsPbI_xBr_{3-x}$ film.

4. Conclusion

In the theoretical study performed here through SCAPS-1D simulations, the performance of the all-inorganic PSCs with inverted structure ITO/i-HTL/$CsPbI_xBr_{3-x}$/i-ETL/Ag has been discussed and optimized. A band gap of 1.78 eV was used for the $CsPbI_xBr_{3-x}$ thin film. Different inorganic materials have been compared as i-HTL (NiO, Cu_2O, CuSCN and CuI) and i-ETL (ZnO, TiO_2 and SnO_2). The simulation results show that CuI as HTL and ZnO as ETL have better performance than the other i-ETL/i-HTL combinations studied. Then, the effects of variation in thicknesses, acceptor densities and defect densities in the perovskite layer on the device performance were simulated for the inverted architecture ITO/CuI/$CsPbI_xBr_{3-x}$/ZnO/Ag. Optimized values of 750 nm and 10^{14} cm^{-3} were obtained for the thickness and acceptor density, respectively. Also, an optimum efficiency of 21.82% could be achieved for this device considering a minority-carrier diffusion length of 10 µm (that is, by reducing the defect density up to 2.07×10^{12} cm^{-3}). The results obtained in this work are very useful to contribute to the design, optimization, and manufacturing process of inverted all-inorganic PSCs and to improve the efficiency of perovskite–perovskite tandem solar cells. Considering that the results obtained through numerical simulation represent a prediction of the behavior of the devices under study, then, the experimental development of promising devices will depend both on the maturity of the technology and on the precise control of the materials involved.

Acknowledgements

This work was partially supported by the National Council Research (CONICET), Argentina, by the Universidad Nacional de Quilmes, Argentina under contract #1303/19, by the Universidad Nacional de La Plata, Argentina, by the Universidad Nacional Arturo Jauretche, Argentina and by the Universidad Nacional del Centro de la Provincia de Buenos Aires, Argentina.

References

Adhikari, K.R., Gurung, S., Bhattarai, B.K., Soucase, B.M., 2016. Comparative study on MAPbI3 based solar cells using different electron transporting materials. Phys. Status Solidi Curr. Top. Solid State Phys. https://doi.org/10.1002/pssc.201510078

Beal, R.E., Slotcavage, D.J., Leijtens, T., Bowring, A.R., Belisle, R.A., Nguyen, W.H., Burkhard, G.F., Hoke, E.T., McGehee, M.D., 2016. Cesium Lead Halide Perovskites with Improved Stability for Tandem Solar Cells. J. Phys. Chem. Lett. https://doi.org/10.1021/acs.jpclett.6b00002

Behrouznejad, F., Shahbazi, S., Taghavinia, N., Wu, H.P., Wei-Guang Diau, E., 2016. A study on utilizing different metals as the back contact of CH3NH3PbI3 perovskite solar cells. J. Mater. Chem. A. https://doi.org/10.1039/c6ta05938d

Burgelman, M., Nollet, P., Degrave, S., 2000. Modelling polycrystalline semiconductor solar cells. Thin Solid Films. https://doi.org/10.1016/S0040-6090(99)00825-1

Burschka, J., Pellet, N., Moon, S.J., Humphry-Baker, R., Gao, P., Nazeeruddin, M.K., Grätzel, M., 2013. Sequential deposition as a route to high-performance perovskite-sensitized solar cells. Nature. https://doi.org/10.1038/nature12340

Cappelletti, M.A., Casas, G.A., Cédola, A.P., Peltzer y Blancá, E.L., Marí Soucase, B., 2018. Study of the reverse saturation current and series resistance of p-p-n perovskite solar cells using the single and double-diode models. Superlattices Microstruct. https://doi.org/10.1016/j.spmi.2018.09.023

Casas, G.A., Cappelletti, M.A., Cédola, A.P., Soucase, B.M., Peltzer y Blancá, E.L., 2017. Analysis of the power conversion efficiency of perovskite solar cells with different materials as Hole-Transport Layer by numerical simulations. Superlattices Microstruct. 107, 136–143. https://doi.org/10.1016/j.spmi.2017.04.007

Chakraborty, K., Choudhury, M.G., Paul, S., 2019. Numerical study of Cs2TiX6 (X = Br−, I−, F− and Cl−) based perovskite solar cell using SCAPS-1D device simulation. Sol. Energy 194, 886–892. https://doi.org/10.1016/j.solener.2019.11.005

Chen, L., Wan, L., Li, X., Zhang, W., Fu, S., Wang, Y., Li, S., Wang, H.Q., Song, W., Fang, J., 2019a. Inverted All-Inorganic CsPbI2Br Perovskite Solar Cells with Promoted Efficiency and Stability by Nickel Incorporation. Chem. Mater. 2–9. https://doi.org/10.1021/acs.chemmater.9b03277

Chen, L., Wan, L., Li, X., Zhang, W., Fu, S., Wang, Y., Li, S., Wang, H.Q., Song, W., Fang, J., 2019b. Inverted All-Inorganic CsPbI2Br Perovskite Solar Cells with Promoted Efficiency and Stability by Nickel Incorporation. Chem. Mater. https://doi.org/10.1021/acs.chemmater.9b03277

Chen, W., Chen, H., Xu, G., Xue, R., Wang, S., Li, Yaowen, Li, Yongfang, 2019. Precise Control of Crystal Growth for Highly Efficient CsPbI 2 Br Perovskite Solar Cells. Joule. https://doi.org/10.1016/j.joule.2018.10.011

Conings, B., Drijkoningen, J., Gauquelin, N., Babayigit, A., D'Haen, J., D'Olieslaeger, L., Ethirajan, A., Verbeeck, J., Manca, J., Mosconi, E., De Angelis, F., Boyen, H.G., 2015. Intrinsic Thermal Instability of Methylammonium Lead Trihalide Perovskite. Adv. Energy Mater. https://doi.org/10.1002/aenm.201500477

Dastidar, S., Li, S., Smolin, S.Y., Baxter, J.B., Fafarman, A.T., 2017. Slow Electron-Hole Recombination in Lead Iodide Perovskites Does Not Require a Molecular Dipole. ACS Energy Lett. https://doi.org/10.1021/acsenergylett.7b00606

Eperon, G.E., Paternò, G.M., Sutton, R.J., Zampetti, A., Haghighirad, A.A., Cacialli, F., Snaith, H.J., 2015. Inorganic caesium lead iodide perovskite solar cells. J. Mater. Chem. A. https://doi.org/10.1039/c5ta06398a

Gao, P., Grätzel, M., Nazeeruddin, M.K., 2014. Organohalide lead perovskites for photovoltaic applications. Energy Environ. Sci. https://doi.org/10.1039/c4ee00942h

Gonzalez-Pedro, V., Juarez-Perez, E.J., Arsyad, W.S., Barea, E.M., Fabregat-Santiago, F., Mora-Sero, I., Bisquert, J., 2014. General working principles of CH3NH3PbX3 perovskite solar cells. Nano Lett. https://doi.org/10.1021/nl404252e

Grätzel, M., 2014. The light and shade of perovskite solar cells. Nat. Mater. https://doi.org/10.1038/nmat4065

Haider, S.Z., Anwar, H., Wang, M., 2019. Theoretical Device Engineering for High-Performance Perovskite Solar Cells Using CuSCN as Hole Transport Material Boost the Efficiency Above 25%. Phys. Status Solidi Appl. Mater. Sci. 216. https://doi.org/10.1002/pssa.201900102

Jiang, Y., Yuan, J., Ni, Y., Yang, J., Wang, Y., Jiu, T., Yuan, M., Chen, J., 2018. Reduced-Dimensional α-CsPbX3 Perovskites for Efficient and Stable Photovoltaics. Joule. https://doi.org/10.1016/j.joule.2018.05.004

Karthick, S., Velumani, S., Bouclé, J., 2020. Experimental and SCAPS simulated

formamidinium perovskite solar cells: A comparison of device performance. Sol. Energy 205, 349–357. https://doi.org/10.1016/j.solener.2020.05.041
Kojima, A., Teshima, K., Shirai, Y., Miyasaka, T., 2009. Organometal halide perovskites as visible-light sensitizers for photovoltaic cells. J. Am. Chem. Soc. https://doi.org/10.1021/ja809598r
Li, B., Zhang, Y., Fu, L., Yu, T., Zhou, S., Zhang, L., Yin, L., 2018. Surface passivation engineering strategy to fully-inorganic cubic CsPbI3 perovskites for high-performance solar cells. Nat. Commun. https://doi.org/10.1038/s41467-018-03169-0
Lin, L., Jiang, L., Li, P., Xiong, H., Kang, Z., Fan, B., Qiu, Y., 2020. Simulated development and optimized performance of CsPbI3 based all-inorganic perovskite solar cells. Sol. Energy 198, 454–460. https://doi.org/10.1016/j.solener.2020.01.081
Liu, C., Li, W., Zhang, C., Ma, Y., Fan, J., Mai, Y., 2018. All-Inorganic CsPbI2Br Perovskite Solar Cells with High Efficiency Exceeding 13%. J. Am. Chem. Soc. https://doi.org/10.1021/jacs.7b13229
Nama Manjunatha, K., Paul, S., 2015. Investigation of optical properties of nickel oxide thin films deposited on different substrates, in: Applied Surface Science. https://doi.org/10.1016/j.apsusc.2015.03.092
NREL, 2020. National Renewable Energy Laboratory Efficiency Chart, September 2020. https://www.nrel.gov/pv/assets/pdfs/best-research-cell-efficiencies.20191104.pdf
Saliba, M., Matsui, T., Domanski, K., Seo, J.Y., Ummadisingu, A., Zakeeruddin, S.M., Correa-Baena, J.P., Tress, W.R., Abate, A., Hagfeldt, A., Grätzel, M., 2016. Incorporation of rubidium cations into perovskite solar cells improves photovoltaic performance. Science (80-.). https://doi.org/10.1126/science.aah5557
Stranks, S.D., Eperon, G.E., Grancini, G., Menelaou, C., Alcocer, M.J.P., Leijtens, T., Herz, L.M., Petrozza, A., Snaith, H.J., 2013. Electron-hole diffusion lengths exceeding 1 micrometer in an organometal trihalide perovskite absorber. Science (80-.). https://doi.org/10.1126/science.1243982
Subhani, W.S., Wang, K., Du, M., Wang, X., Liu, S. (Frank), 2019. Interface-Modification-Induced Gradient Energy Band for Highly Efficient CsPbIBr2 Perovskite Solar Cells. Adv. Energy Mater. https://doi.org/10.1002/aenm.201803785
Sutton, R.J., Eperon, G.E., Miranda, L., Parrott, E.S., Kamino, B.A., Patel, J.B., Hörantner, M.T., Johnston, M.B., Haghighirad, A.A., Moore, D.T., Snaith, H.J., 2016. Bandgap-Tunable Cesium Lead Halide Perovskites with High Thermal Stability for Efficient Solar Cells. Adv. Energy Mater. https://doi.org/10.1002/aenm.201502458
Swarnkar, A., Marshall, A.R., Sanehira, E.M., Chernomordik, B.D., Moore, D.T., Christians, J.A., Chakrabarti, T., Luther, J.M., 2016. Quantum dot-induced phase stabilization of α-CsPbI3 perovskite for high-efficiency photovoltaics. Science (80-.). https://doi.org/10.1126/science.aag2700
Tao, S., Schmidt, I., Brocks, G., Jiang, J., Tranca, I., Meerholz, K., Olthof, S., 2019. Absolute energy level positions in tin- and lead-based halide perovskites. Nat. Commun. https://doi.org/10.1038/s41467-019-10468-7
Tian, J., Xue, Q., Tang, X., Chen, Y., Li, N., Hu, Z., Shi, T., Wang, X., Huang, F., Brabec, C.J., Yip, H.L., Cao, Y., 2019. Dual Interfacial Design for Efficient CsPbI2Br Perovskite Solar Cells with Improved Photostability. Adv. Mater. https://doi.org/10.1002/adma.201901152
Wang, J., Zhang, J., Zhou, Y., Liu, H., Xue, Q., Li, X., Chueh, C.C., Yip, H.L., Zhu, Z., Jen, A.K.Y., 2020. Highly efficient all-inorganic perovskite solar cells with suppressed non-radiative recombination by a Lewis base. Nat. Commun. 11, 1–9. https://doi.org/10.1038/s41467-019-13909-5
Wang, Q., Zheng, X., Deng, Y., Zhao, J., Chen, Z., Huang, J., 2017. Stabilizing the α-Phase of CsPbI3 Perovskite by Sulfobetaine Zwitterions in One-Step Spin-Coating Films. Joule. https://doi.org/10.1016/j.joule.2017.07.017
Wang, Y., Liu, X., Zhang, T., Wang, X., Kan, M., Shi, J., Zhao, Y., 2019. The Role of Dimethylammonium Iodide in CsPbI3 Perovskite Fabrication: Additive or Dopant? Angew. Chemie - Int. Ed. https://doi.org/10.1002/anie.201910800
Yang, Y., You, J., 2017. Make perovskite solar cells stable. Nature.

https://doi.org/10.1038/544155a
Zhang, S., Wu, S., Chen, Weitao, Zhu, H., Xiong, Z., Yang, Z., Chen, C., Chen, R., Han, L., Chen, Wei, 2018. Solvent engineering for efficient inverted perovskite solar cells based on inorganic CsPbI2Br light absorber. Mater. Today Energy. https://doi.org/10.1016/j.mtener.2018.03.006
Zhao, Y., Duan, J., Yuan, H., Wang, Y., Yang, X., He, B., Tang, Q., 2019. Using SnO2 QDs and CsMBr3 (M = Sn, Bi, Cu) QDs as Charge-Transporting Materials for 10.6%-Efficiency All-Inorganic CsPbBr3 Perovskite Solar Cells with an Ultrahigh Open-Circuit Voltage of 1.610 V. Sol. RRL. https://doi.org/10.1002/solr.201800284